Characterizing high-n quasi-one-dimensional strontium Rydberg atoms

M. Hiller,[1,2] S. Yoshida,[1] J. Burgdörfer,[1] S. Ye,[3] X. Zhang,[3] and F. B. Dunning[3]
[1]*Institute for Theoretical Physics, Vienna University of Technology, Vienna, Austria, EU*
[2]*Physikalisches Institut, Albert-Ludwigs-Universität Freiburg, Freiburg, Germany, EU*
[3]*Department of Physics and Astronomy and the Rice Quantum Institute, Rice University, Houston, Texas 77005-1892, USA*
(Received 28 November 2013; revised manuscript received 30 January 2014; published 21 February 2014)

The production of high-n, $n \sim 300$, quasi-one-dimensional (quasi-1D) strontium Rydberg atoms through two-photon excitation of selected extreme Stark states in the presence of a weak dc field is examined using a crossed laser-atom beam geometry. The dipolar polarization of the electron wave function in the product states is probed using two independent techniques. The experimental data are analyzed with a classical trajectory Monte Carlo simulation employing initial ensembles that are obtained with the aid of quantum calculations based on a two-active-electron model. Comparisons between theory and experiment highlight different characteristics of the product quasi-1D states, in particular, their large permanent dipole moments, $\sim$1.0 to $1.2n^2ea_0$, where e is the electronic charge and a_0 is the Bohr radius. Such states can be engineered using pulsed electric fields to create a wide variety of target states.

DOI: 10.1103/PhysRevA.89.023426 PACS number(s): 32.80.Ee, 32.80.Rm, 32.60.+i

I. INTRODUCTION

As demonstrated in earlier studies using $n \sim 300$ potassium Rydberg atoms, the production of strongly polarized quasi-one-dimensional (quasi-1D) Rydberg states provides a valuable gateway to studies of nonlinear dynamics and chaos in the ultrafast, ultraintense regime [1–3] and to the control and manipulation of excited electronic states, including the creation of states in which the electron moves about the nucleus in a near-circular "Bohr-like" orbit [4–6]. Notwithstanding the wealth of new insights obtained using alkali metals, the alkaline-earth elements offer the opportunity to explore new aspects of Rydberg atom physics [7–9]. For example, in the case of high total angular momentum Rydberg states, the presence of the second valence electron leaves a readily excited, optically active core ion that can be manipulated through optical trapping or imaged through laser-induced fluorescence [10]. The second valence electron also admits the possibility of creating quasistable two-electron-excited states with the planetary atom [11] or frozen planet configurations [12,13]. To fully exploit these opportunities, however, requires the creation of quasi-1D strontium Rydberg atoms and the application of techniques developed previously to engineer their properties using one or more pulsed electric fields [1,5].

Generally, quasi-1D Rydberg states can be created by exciting the lowest-lying states in a particular Stark manifold in the presence of a weak dc field [14]. For hydrogen, the degeneracy in the unperturbed energy levels is removed by a dc field, the various states displaying linear Stark shifts. The extreme eigenstates are strongly polarized and have large electric dipole moments. Due to field-induced angular momentum mixing, each eigenstate is a superposition of many unperturbed ℓ states. As n increases so too does the number of ℓ states involved, which limits the contribution from low-ℓ states. As a consequence, the oscillator strengths for few-photon excitation are small and photoexcitation is, typically, inefficient. The situation is different for alkali- or alkaline-earth atoms, for which quantum defects shift the energies of the low-ℓ states. Initially these nondegenerate states display, to leading order, a quadratic Stark effect, indicating that, at least in modest applied fields, they are only weakly polarized. On the other hand, because of their weak ℓ mixing, relatively large oscillator strengths are maintained even in the presence of a dc field. In the present work, we analyze the transition of an isolated low-ℓ state into a Stark state in the quasihydrogenic limit as the dc field strength is increased. The goal is to determine an effective pathway to create quasi-1D states that are well polarized and yet still feature a reasonably large oscillator strength. Two independent techniques are employed to probe the polarization (i.e., dipole moment) of the electronic wave function. These were originally developed for alkali atoms and comprise pulsed field ionization [14,15] and the production of circular wave packets [16]. The applicability of these methods to a system with two active electrons, such as strontium, is examined. Detailed comparison of results obtained using these methods illuminates the degree of ℓ mixing in the product states and its role in the ionization processes.

Despite the presence of a second valence electron, strontium is a good candidate to apply the same techniques as employed using alkali atoms to excite quasi-1D states. Few perturbers (doubly excited states) are found below the first ionization threshold, and these only influence the energy of singly excited states below $n = 20$ [17]. High-lying, singly excited strontium Rydberg states thus closely resemble alkali Rydberg atoms [18,19]. While high-n potassium quasi-1D states have been (typically) produced by single-photon excitation from the ground state, a (sequential) two-photon excitation scheme utilizing the intermediate $5s5p\ ^1P_1$ state is preferred for the production of quasi-1D strontium atoms. By saturating the transition to the $5s5p\ ^1P_1$ state, the final Rydberg production rate can be increased relative to single-photon excitation. Since two-photon excitation leads to different selection rules, the characteristics of the product states differ from those generated by single-photon excitation. The resulting polarization of the excited states is carefully examined in the following.

The outline of the present paper is as follows. The current experimental apparatus is described in Sec. II. In the subsequent sections we review the theoretical models used

to describe the excitation process, which are based on the two-active-electron (TAE) model [20] (Sec. III), and the classical ionization dynamics underlying the probing techniques (Sec. IV). In Sec. V, we introduce a representation of isolated strontium low-L states in the presence of a weak dc field in terms of a classical initial phase-space distribution, which serves as a starting point for our classical trajectory Monte Carlo simulations of the ionization dynamics. In Sec. VI, results obtained using the two probing protocols are discussed and compared with experiment. We conclude with a summary in Sec. VII.

II. EXPERIMENTAL APPROACH

The present apparatus is shown in Fig. 1. Briefly, strontium atoms contained in a tightly collimated beam are excited to the desired high-n singlet state using the crossed outputs of two frequency-doubled diode laser systems. The two-photon excitation scheme employed, which is diagramed in the inset in Fig. 1, utilizes the intermediate $5s5p\ ^1P_1$ state and radiation at 461 nm and 413 nm. The laser beams, which are both linearly polarized along the z axis as indicated, cross the atom beam traveling in opposite directions. Since their wavelengths are comparable, the use of counterpropagating light beams can largely cancel Doppler effects associated with atom beam divergence, resulting in narrow effective experimental linewidths, ~5 MHz. The strontium atom beam is provided by an oven that can, with appropriate collimation, provide a beam with a full width at half maximum divergence of ~4 mrad at densities approaching 10^9 cm^{-3}. As described elsewhere, residual stray fields in the experimental volume are reduced to $\leqslant 50\ \mu$V cm^{-1} by application of small offset potentials to the electrodes that surround it [1].

Measurements are conducted in a pulsed mode. The output of the 461-nm laser is chopped into a series of pulses of 0.5-μs duration and 20 kHz pulse repetition frequency using an acousto-optic modulator. (The 413-nm radiation remains on at all times.) Excitation occurs in the presence of the dc Stark field, $F_{\rm dc}$. Following excitation, the electric polarization of the product states is examined through ionization induced by application of a short electric field pulse, either parallel or antiparallel to the polarization axis. As will be shown, the asymmetry present in the resulting survival probabilities provides a sensitive probe of the polarization of the initial states. Alternately, a transverse electric field pulse is applied to convert the initial state into a near-circular state whose subsequent evolution is monitored using a further probe pulse. The probability that a Rydberg atom survives the probe pulse(s) is determined by state-selective field ionization, for which purpose a slowly rising (rise time ~1 μs) electric field is generated in the experimental volume by applying a positive voltage ramp to the lower electrode. Product electrons are accelerated out of the interaction region and are detected by a particle multiplier. The number of Rydberg atoms initially created is monitored through periodic measurements in which no pulsed fields are applied, thereby allowing survival probabilities (or ionization fractions) to be determined.

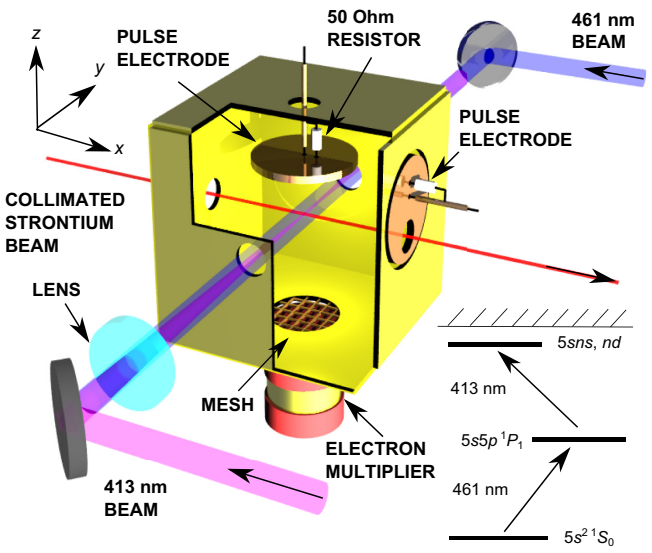

FIG. 1. (Color online) Schematic diagram of the apparatus. The inset shows the two-photon excitation scheme employed.

III. EFFECTIVE TWO-ELECTRON ATOMS IN A DC ELECTRIC FIELD

A. Quantum description

For reference, we start by briefly reviewing the basic properties of atoms with a single active electron when subject to a weak dc electric field $F_{\rm dc}$ directed along the z axis [21,22]. Attention is then turned to atoms featuring two active electrons that move in a mean field provided by the core electrons. For the single-active-electron (SAE) model, the Hamiltonian is given by

$$H = \frac{p^2}{2} + V(r) + zF_{\rm dc} \tag{1}$$

and the eigenstates are formed from superpositions of angular momentum (ℓ) states. (Atomic units are used throughout, unless otherwise noted.) In particular, for hydrogenic atoms, i.e., $V(r) = -1/r$, the eigenstates in the linear Stark regime are approximated by parabolic states

$$|\phi_{n,k,m}\rangle = \sum_{\ell} C_{n,m}(k,\ell)|\varphi_{n,\ell,m}\rangle \tag{2}$$

with eigenenergies

$$E^{\rm H}_{n,k} = -\frac{1}{2n^2} + \frac{3}{2}nkF_{\rm dc}. \tag{3}$$

The expansion coefficients $C_{n,m}(k,\ell)$ are the Clebsch-Gordan coefficients expressed in terms of Wigner $3j$ symbols as

$$C_{n,m}(k,\ell) = (-1)^m\sqrt{2\ell+1}\begin{pmatrix}(n-1)/2 & (n-1)/2 & \ell\\ (m+k)/2 & (m-k)/2 & -m\end{pmatrix}. \tag{4}$$

The quantum number k is proportional to the quantized action of the Runge-Lenz vector A projected along the z axis ($k = -nA_z$) and therefore represents the degree of atomic polarization along the dc field axis, i.e., $\langle d\rangle = -(3/2)nk$. The

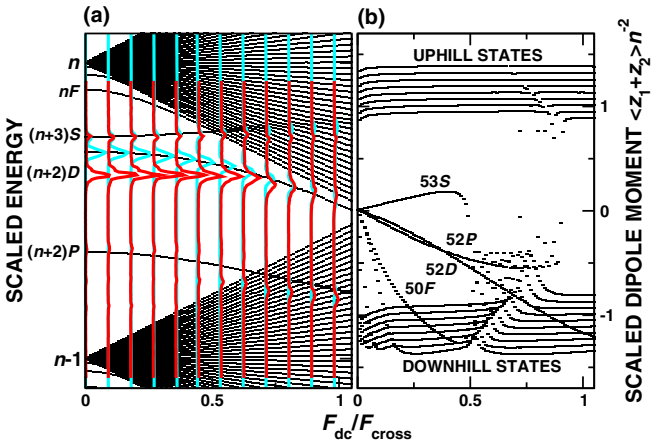

FIG. 2. (Color online) (a) Evolution of the measured excitation spectrum of strontium with increasing applied dc field $F_{\rm dc}$ for $M = 0$ states in the vicinity of $n \sim 274$ [thick red (dark grey) lines]. The thin solid black lines show the calculated Stark energy level structure for singly excited strontium near $n \sim 50$, and the thick blue (light grey) lines denote calculated excitation spectra. The applied field is normalized to the crossing field $F_{\rm cross}$ (see text), i.e., $F_0 = F_{\rm dc}/F_{\rm cross}$. The energy axis is scaled such that $E_0 = 1$ corresponds to the energy difference between neighboring n and $(n-1)$ manifolds. (b) Field dependence of the calculated average scaled dipole moment for low-L states and selected extreme blue-shifted (uphill) and red-shifted (downhill) Stark states.

maximally polarized states [$|\langle d\rangle| \simeq (3/2)n^2$] are optically accessible from the ground s state. For single-photon excitation, the dipole transition matrix elements can be evaluated as

$$\langle \phi_{n,n-1,m}|z|{\rm g}\rangle = C_{n,m}(k = n-1, \ell = 1)\langle \varphi_{n,\ell=1,m}|z|{\rm g}\rangle, \quad (5)$$

where $|{\rm g}\rangle$ denotes the ground state. Due to the strong ℓ mixing induced by the dc field, the low-ℓ contributions to the highly polarized states are relatively small. For high n, the excitation probability scales as $\sim n^{-5}$ (i.e., $\langle \varphi_{n,\ell=1,m}|z|{\rm g}\rangle \sim n^{-3/2}$ and $C_{n,m}(k = n-1, \ell = 1) \sim n^{-1}$ [23,24]), and therefore decreases rapidly with n, hindering the efficient production of the high-n polarized states.

Alkaline-earth atoms, however, display a rather different behavior. In the case of strontium, the ratio of low-L to high-L states is significantly increased by the presence of the second valence electron. This can be clearly seen in the calculated Stark spectrum for the $M = 0$ strontium manifold in the vicinity of $n \sim 50$ [Fig. 2(a)]. (In the following, L indicates the total orbital angular momentum while ℓ denotes that of a single electron.) This calculation employs the TAE model described in more detail elsewhere [20]. Briefly, the Hamiltonian

$$H = \frac{p_1^2}{2} + V_{\ell_1}(r_1) + \frac{p_2^2}{2} + V_{\ell_2}(r_2) + \frac{1}{|\vec{r}_1 - \vec{r}_2|} + (z_1 + z_2)F_{\rm dc}, \quad (6)$$

where the ℓ-dependent model potential $V_\ell(r)$ representing the Sr^{2+} ion, taken from [25], is diagonalized in a large truncated basis built up from angular-momentum-coupled product states of single-particle orbitals for the Sr^+ ion. Such an approach corresponds to a configuration-interaction (CI) calculation for a quasi-two-electron system. The calculated Stark spectrum [Fig. 2(a)] in the singlet sector displays isolated low-L ($L = 0,1,2$, and 3) states at zero dc field. The calculated quantum defects μ_L agree well with the measured values [26,27]. The small discrepancies in the D state peak positions as compared to experimental measurements are partly due to n dependences in the quantum defect ($n \simeq 50$ for the theory and $n \simeq 274$ for the experiment) and partly due to the inaccuracy of the model potential [20]. The low-L states experience an energy shift which, to leading order, is initially quadratic in $F_{\rm dc}$. For small $F_{\rm dc}$, their calculated dipole moments thus increase linearly with $F_{\rm dc}$ [see Fig. 2(b)], indicating that the corresponding field-perturbed eigenstates are superpositions involving only the dipole-coupled states [20]. This is to be contrasted with the parabolic states, which involve all angular momentum states and have a constant dipole moment determined by the Clebsch-Gordan coefficients [Eq. (2)]. Consequently, when strontium is excited from the intermediate $5s5p\ ^1P_1$ state in the presence of a dc field, the oscillator strength is not broadly distributed over all angular momentum states but is rather shared among a smaller number of dipole-coupled low-L states.

The relative oscillator strengths displayed in Fig. 2(a) are determined from the squared dipole transition matrix element between the excited Rydberg state and the intermediate $5s5p\ ^1P_1$ state. Due to the dipole selection rules, at $F_{\rm dc} = 0$ only the S and D states have finite oscillator strength. With increasing $F_{\rm dc}$, the P and F states acquire finite excitation probability while the peak heights for the S and D states decrease. As the field strength approaches the value

$$F_{\rm cross} \simeq \frac{1}{3n^5} \quad (7)$$

at which two adjacent n-manifolds first cross, the D (and F) states become indistinguishable from the parabolic states, indicating that they have reached the quasihydrogenic limit. The field-perturbed "D" state therefore provides an opportunity to efficiently excite quasi-1D states in fields $F_{\rm dc} \lesssim F_{\rm cross}$.

B. Classical analysis of the spectrum

Because the dominant CI configuration is, by far, the $|5sn\ell\rangle$ configuration, many features of the spectrum can be qualitatively accounted for within an SAE model. Moreover, since the outer $n\ell$ orbitals are in the quasiclassical regime, we can invoke classical dynamics for the active electron to discuss qualitatively the quantum states described above.

In the hydrogenic limit, corresponding to $V(r) = -1/r$ in Eq. (1), the secular motion of electron orbits in a weak dc field can be described by the equations [28]

$$\frac{d}{dt}\vec{\ell}_T = \frac{3}{2}n^2 F_{\rm dc}\vec{A}_T \times \hat{z}, \quad \frac{d}{dt}\vec{A}_T = \frac{3}{2}F_{\rm dc}\vec{\ell}_T \times \hat{z}, \quad (8)$$

where the angular momentum $\vec{\ell}_T$ and the Runge-Lenz vector $\vec{A}_T$ of the (outer) electron are averaged over the orbital period. Analogous to a parabolic quantum state, the corresponding classical ensemble has three well-defined actions ($n, k = -nA_{T,z}, m = \ell_{T,z}$). Both vectors precess about the field (z) axis, i.e., their x and y components oscillate sinusoidally and the magnitude ℓ evolves in time [see Figs. 3(d) and 3(e)]. For later reference, we note that restricted microcanonical

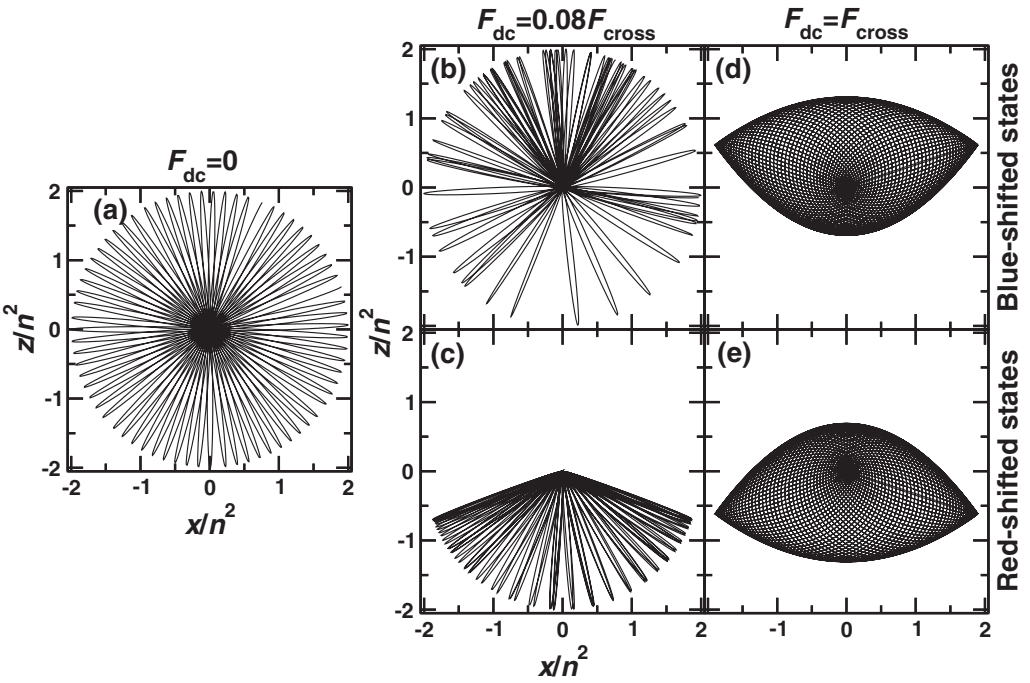

FIG. 3. Classical trajectories of an excited electron for (a) strontium in the absence of external fields, (b),(c) strontium with $F_{\rm dc} = 0.4$ V/cm $\simeq 0.08 F_{\rm cross}$, and (d),(e) hydrogen with $F_{\rm dc} = 5$ V/cm $\simeq F_{\rm cross}$. (b),(d) and (c),(e) relate to blue-shifted and red-shifted orbits, respectively. The initial conditions correspond to the $n = 50$ D-state ($L = 2$) and the dynamics is generated by the SAE model potential Eq. (9). $\vec{\ell}$ is parallel to the y axis and $F_{\rm dc}$ is directed along the z axis.

ensembles sampled from such (quasi-)periodic orbits are often used as a classical approximation to a parabolic state [Eq. (2)].

For nonhydrogenic systems, the excited electron can penetrate the orbitals of core electrons and scattering by the core electrons [22] becomes important, giving rise to quantum defects. Since for highly excited strontium atoms the inner electron is almost exclusively in the $5s$ state, the core potential $V(r)$ in Eq. (1) can be approximated by a spherically symmetric potential. Here we employ the SAE approximation and the following ℓ-dependent model potential:

$$V_\ell^{\rm SAE}(r) = -\frac{1}{r}\left[1 + 37\exp\left(-\alpha_1^\ell r\right) + \alpha_2^\ell r\,\exp\left(-\alpha_3^\ell r\right)\right] - \frac{\alpha_{\rm cp}}{2r^4}\left[1 - \exp\left[-\left(r/r_c^\ell\right)^6\right]\right], \tag{9}$$

where the parameters (Table I) are fitted to yield the correct quantum defects at high n (>20). For the noninteger values of ℓ appearing in the classical simulations, the ℓ-dependent parameters are interpolated.

TABLE I. Model potential parameters for the SAE approximation of neutral strontium, Eq. (9). The parameters are chosen to yield the correct quantum defects for highly excited states ($n > 30$).

ℓ	α_1^ℓ	α_2^ℓ	α_3^ℓ	$\alpha_{\rm cp}$	r_c^ℓ
0	3.361 24	5.943 37	1.3337	7.5	1.59
1	3.282 05	3.788 61	1.240 35	7.5	1.58
2	2.155	4.5111	1.4545	7.5	1.57
$\geqslant 3$	2.1547	2.1987	1.140 99	7.5	1.56

In the absence of $F_{\rm dc}$, the spherically symmetric potential preserves the angular momentum $\vec{\ell}$. However, in contrast to the case for a pure Coulomb potential, the Runge-Lenz vector $\vec{A}$ is not constant but precesses around the $\vec{\ell}$ axis [Fig. 3(a)]. The rate of this core-induced precession can be calculated within the framework of secular perturbation theory as [22]

$$\omega_c \simeq \frac{1}{n^3}(\mu_\ell - \mu_{\ell+1}). \tag{10}$$

Core-induced precession is non-negligible for low-ℓ states ($\ell \leqslant 3$) because their inner turning points are close to the core. We note that the estimate for ω_c is based on lowest-order perturbation theory relative to the unperturbed Kepler motion. For strontium, however, ω_c is comparable or even larger than the Kepler orbital frequency ($1/n^3$). Thus, while Eq. (10) qualitatively captures the perturbed classical dynamics, it is unreliable for a quantitative description. Moreover, since the quantum defects are large, the classical limit of quantum dynamics may not yet be reached. Upon application of a weak field $F_{\rm dc}$, the orbits tend to become oriented, i.e., polarized, along the field (z) axis. However, precession induced by core scattering tends to randomize this orientation, reducing the polarization and providing a classical explanation for the absence of a linear Stark effect. As $F_{\rm dc}$ increases, the distribution of their orientations becomes increasingly aligned with respect to the field direction, leading to a (weakly) polarized ensemble [see Figs. 3(b) and 3(c)]. Also, the magnitude ℓ evolves in time but only with small fluctuations around the initial value. Thus the ensemble of core-scattered ellipses in Figs. 3(b) and 3(c) have nearly the same eccentricity. Only when the precession induced by $F_{\rm dc}$ dominates over that

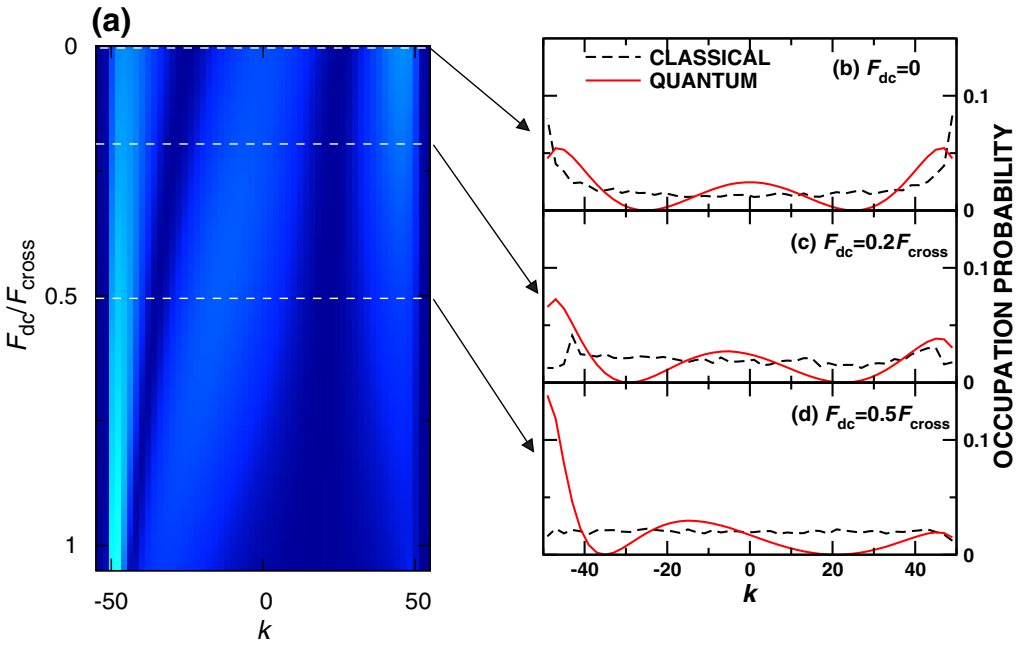

FIG. 4. (Color online) (a) Quantum probability distribution $\rho_{qm}(k)$ [Eq. (11)] of the parabolic quantum number $k(=-nA_z)$ for the $M=0$ "$52D$" state as a function of applied dc field normalized as in Fig. 2. (b)–(d) Cuts through the distribution in (a) for the selected values of F_{dc} indicated. These are compared to the classical distribution $\rho_{cl}(k)$ (see text).

induced by core scattering can the ensemble be approximated by a hydrogenic parabolic state as in Figs. 3(d) and 3(e). As suggested by the quantum Stark map [see Fig. 2(a)], this crossover is reached when $F_{dc} \simeq F_{cross}$.

The evolution of the ensemble of classical orbits as a function of the applied field can be compared and contrasted with the corresponding evolution of the quantum state. We consider the reduced distribution function $\rho_{qm}(k)$ in the parabolic quantum number k after tracing out the principal quantum number,

$$\rho_{qm}(k) = \sum_n |\langle 5sn\ell; LM=0|\varphi_{500};\phi_{n,k,0}\rangle|^2 . \qquad (11)$$

$\langle 5sn\ell; LM=0|$ denotes the eigenstates calculated using the TAE model, while $|\varphi_{500}\rangle$ denotes the $5s$ inner electron state and $|\phi_{n,k,0}\rangle$ the hydrogenic parabolic state of the outer electron. As demonstrated in Fig. 4, at small fields, $F_{dc} \approx 0$, the distribution $\rho_{qm}(k)$ for the $52D$ state is broad, reflecting the spread of A_z and the weak polarization of the electron wave function. As F_{dc} increases the distribution in k becomes increasingly asymmetric and converges to a narrow distribution of extreme parabolic states as F_{dc} nears F_{cross}, indicating strong polarization. Here, and in the following, "nL" is used to denote the perturbed state (in the presence of the dc field) associated with an unperturbed nL state.

It is of conceptual interest to compare the quantum distribution $\rho_{qm}(k)$ determined from the dominant CI configurations with a classical distribution $\rho_{cl}(k)$ derived from a restricted microcanonical ensemble in a dc field. In order to mimic the initial photoexcitation to the "$52D$" state, only initial phase-space coordinates within 20 a.u. of the core are selected from the microcanonical ensemble of the $52D$ state. After allowing evolution for a duration of 4.4 ns (more than 200 orbital periods), the k distribution $\rho_{cl}(k)$ is extracted [see Figs. 4(b)–4(d)]. At low F_{dc}, both $\rho_{qm}(k)$ and $\rho_{cl}(k)$ are broad, although the nodal lines associated with the quantum "D" state are absent from the classical distribution. With increasing F_{dc}, the quantum distribution becomes increasingly polarized, as evidenced by the growing peak at $k \simeq -50$, whereas the classical distributions fail to reproduce any such peak. This biased k distribution gives rise to the quadratic energy shifts seen in Fig. 2(a) for the "$52D$" state, which results from the superposition of a few low-L states. The shifts are missing in the classical distribution $\rho_{cl}(k)$ due to the dominance of low-L states in this regime for which quantum-classical correspondence is not expected to hold. Only in the near-parabolic limit, $F_{dc} \sim F_{cross}$, which involves a high density of high-L states, will the correspondence be restored. Therefore, in the classical simulations of the ionization induced by a probe pulse to be discussed below, we use $\rho_{qm}(k)$ rather than $\rho_{cl}(k)$ as input.

IV. PROBING THE POLARIZATION

Since the photoexcited Stark states furnish the starting point for Rydberg state manipulation and engineering, accurate characterization of their polarization is critical. While the dipole moment of Stark states can be easily determined numerically, this is not a trivial task experimentally. In this section, we briefly review two independent methods for probing the polarization of strontium Rydberg states that are based on techniques originally developed for hydrogenic atoms. In each approach, probe pulses are used to ionize the atom and the resulting ionization (or survival) probabilities are mapped to the polarization (i.e., the electric dipole moment)

of the initial Rydberg state. Since the singly excited Rydberg states of strontium have only weak correlations among the valence electrons, we expect that probing techniques devised for potassium Rydberg atoms should work reasonably well. We compare results obtained using each probing protocol to highlight the properties of the targeted states. The intuitive understanding of each probing scheme is aided by classical simulations of the ionization dynamics.

A. Pulsed field ionization

When a hydrogenic atom is subject to a field step,

$$\vec{F}_{\text{step}}(t) = \begin{cases} F_{\text{step}}\hat{z} & 0 \leqslant t \leqslant T_{\text{step}} \\ 0 & \text{otherwise} \end{cases}, \tag{12}$$

the electron can be ionized provided that the field strength F_{step} is sufficiently large. If the electron wave function is polarized, the ionization probability depends markedly on whether the probe field is applied parallel or antiparallel to the dipole moment of the atom. This asymmetry in the ionization dynamics provides a simple tool with which to examine the polarization of the Rydberg state.

Assuming the pulse duration T_{step} to be infinitely long, the classical overbarrier ionization condition is given analytically [15,21] by

$$2E_i z_i + F_{\text{step}} r_i^2 < -\frac{E_i^2}{F_{\text{step}}} + 2(1 + A_{zi}), \tag{13}$$

where the index i indicates the initial value of the observables at $t = 0$, i.e., at the time of application of the field step. It is, in general, not straightforward to extract information on the z coordinate, because ionization depends on four different parameters, E_i, r_i, z_i, A_{zi}. In a few important cases, however, Eq. (13) can be used to probe the average position of the wave function, i.e., of the classical ensemble. In the case of circular orbits (i.e., high-ℓ states), the ionization condition depends solely on z_i [16] as three of the parameters are constant $E_i = -1/(2n^2)$, $r_i = n^2$, $A_{zi} = 0$. This is exploited in the second probing scheme.

For an extreme parabolic state, all members of the corresponding classical ensemble have the same energy, $E_i = -1/(2n^2)$, in the absence of an external field. Additionally, the elongated electron orbits can be approximated by $z_i \simeq +r_i$ and $-r_i$ and $A_{zi} \simeq -1$ and $+1$ for the extreme uphill (blue-shifted) and the downhill (red-shifted) states, respectively. By setting $F_{\text{step}} > 0$, the ionization condition [Eq. (13)] can be simplified as

$$\begin{cases} (E_i + F_{\text{step}} r_i)^2 < 0 & \text{for uphill states} \\ (E_i - F_{\text{step}} r_i)^2 < 4F_{\text{step}} & \text{for downhill states} \end{cases}. \tag{14}$$

This inequality indicates that ionization is suppressed for the uphill electron states (with energy $E_i + F_{\text{step}} r_i$) relative to downhill electron states (with energy $E_i - F_{\text{step}} r_i$). The field strengths required for ionization are smallest for the downhill states when the electron is near the origin ($r_i \to 0$), the threshold value, $F_{\text{step}} > 1/(16n^4)$, matching the well-known classical value. Downhill states are easier to ionize because their ellipses extend from the nucleus towards the Stark saddle point [see Fig. 5(a)] formed in the presence of the probe field, thus allowing a quick escape over the barrier, as indicated by the red trajectory in Fig. 5(b). In contrast, uphill trajectories are oriented away from the saddle point and, as shown by the green trajectory in Fig. 5(b), do not escape in the absence of additional perturbations. When the initial elliptic orbit and the z axis are misaligned by an angle θ_i, i.e., $z_i = r_i \cos\theta_i$, the precession induced by the probe field can, in principle, bring an electron initially located on the uphill side (i.e., $\cos\theta_i > 0$) towards the saddle point and hence induce ionization. The decomposition of phase space into ionizing and nonionizing regimes is displayed for low-ℓ Rydberg states in the $(r_i/n^2, \cos\theta_i)$ plane in Fig. 6. While for ellipses aligned on the uphill side ($\cos\theta_i > 0$) survival dominates, ionization prevails on the downhill side ($\cos\theta_i < 0$). Whereas the above discussion applies to low-ℓ states, high-ℓ states display similar

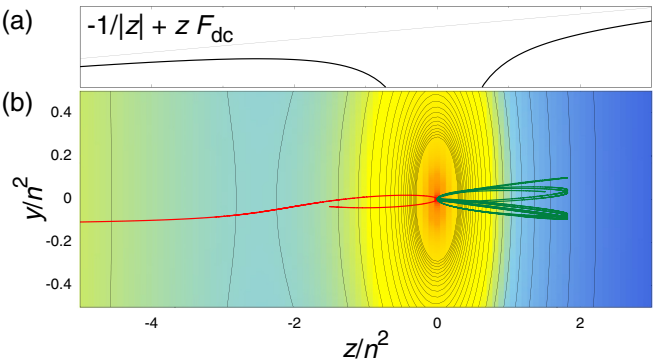

FIG. 5. (Color online) (a) Coulomb potential as modified by a dc field F_{dc}. (b) Contour plot of the energy surface $E = -1/r + zF_{\text{dc}}$. A low-$\ell$ trajectory on the downhill side (red line) is rapidly ionized over the Stark saddle, whereas one on the uphill side (green line) remains remote from the saddle and is not ionized.

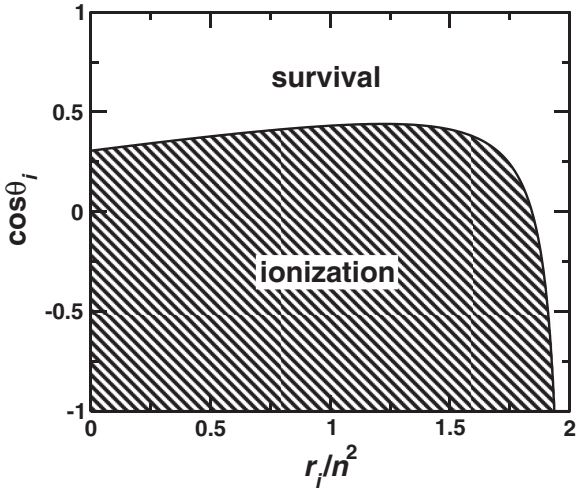

FIG. 6. Ionization behavior [Eq. (13)] of low-ℓ ($\ell_i \sim 0$) Rydberg states subject to a field step (see text). The electron is initially located at $z_i \simeq r_i \cos\theta_i$. The electron energy and the field amplitude are given by $E_i = -1/(2n^2)$ and $F_{\text{step}} = 0.17/n^4$.

tendencies but the asymmetry is expected to be smaller. With increasing ℓ, the elliptic orbits on the uphill side extend further towards the downhill side, increasing the probability for the electron to escape over the Stark saddle. While the present analysis of ionization dynamics assumes a hydrogenlike atom, this is justified because a strong probe field ($F_{\rm step} \sim 200 F_{\rm cross}$) is typically employed to ensure sizable ionization probabilities. Under such strong fields low-ℓ states evolve quickly into high-ℓ states due to field-induced precession [Eq. (8)], which dominates over core-induced precession.

B. Production of circular wave packets

Quasi-1D atoms can serve as a starting point for engineering wave packets that travel in near-circular "Bohr-like" orbits [5,16]. By monitoring the properties of the resulting Bohr-like wave packets, detailed information on the initial state can be extracted [29]. Here, we employ such circular wave packets to characterize the polarization of the initially prepared Rydberg state.

To create a circular state from (in this case) a high-n state polarized along the z axis, a transverse "pump field" polarized along the x axis,

$$\vec{F}_{\rm pump}(t) = \begin{cases} F_{\rm pump}\,\hat{x} & \text{when} \quad 0 \leqslant t \leqslant T_{\rm pump} \\ 0 & \text{otherwise} \end{cases}, \qquad (15)$$

is applied. The orbit follows the Bloch equations [Eq. (8)] for precessional motion, with $\omega_S = (3/2)nF_{\rm pump}$ being the Stark precession frequency. A strongly polarized Rydberg state, $\vec{\ell}_T(0) \simeq 0$ (i.e., $\ll n$) and $\vec{A}_T(0) \simeq \hat{z}$ [see also Fig. 7(a)], is transformed to a circular state, with $\ell_{T,y}(T_{\rm pump}) \simeq n$ confined to the xz plane at $T_{\rm pump} = \pi/(2\omega_S)$. If the initial state is polarized but misaligned from the z axis by an angle θ [i.e., $A_{T,z}(0) = -k/n = A_0 \cos\theta$ and $A_{T,y}(0) = -A_0 \sin\theta$], the final angular momentum at $t = T_{\rm pump}$ becomes

$$\vec{\ell}_T(T_{\rm pump}) \simeq \begin{pmatrix} \ell_{T,x}(0) \\ nA_{T,z}(0) \\ -nA_{T,y}(0) \end{pmatrix}. \qquad (16)$$

The resulting orbit has the well-defined value of $\ell_{T,y}(T_{\rm pump}) = nA_0 \cos\theta$. Since $\ell_{T,z}(T_{\rm pump}) = nA_0 \sin\theta$ is finite, the circular orbit is not confined to the xz plane but tilted by an angle θ about the x axis [see Fig. 7(b)]. If the initial state is strongly polarized but is oriented along the $-z$ axis, it is again transformed to a circular orbit in the xz plane but with $\ell_{T,y}(T_{\rm pump}) \simeq -n$ [see Fig. 7(c)]. The distribution of orbital planes after application of the pump field can be used to extract information on the initial degree of polarization as follows: if the initial state is an unperturbed low-ℓ state, the θ distribution of the associated classical ensemble, i.e., the distribution of the orientations of the Kepler ellipses, is symmetric under reflection at the origin, i.e., under the transformation $\vec{A}_T(0) \to -\vec{A}_T(0)$. This results in a vanishing dipole moment $\langle \vec{d}(0) \rangle = (3/2)n^2 \langle \vec{A}_T(0) \rangle = 0$. The distribution of $\vec{\ell}_T(0)$, however, need not be symmetrically distributed, as is the case, for example, for states with a finite $m = \langle \ell_{z,T}(0) \rangle$. The angular momentum vectors of the near-circular orbits after the pump pulse, i.e., at $t = T_{\rm pump}$, inherit the symmetry of the Runge-Lenz vector distribution at $t = 0$ but only in their y and z components [Eq. (16)]. As illustrated in Fig. 7, only for low-ℓ states where the x component vanishes [$\ell_{T,x}(T_{\rm pump}) \simeq \ell_{T,x}(0) \simeq 0$] are the angular momentum vectors $\vec{\ell}_T(T_{\rm pump})$ confined close to the yz plane and symmetrically distributed. However, in the presence of a weak dc field $F_{\rm dc}$, the ensemble representing the initial field-perturbed low-ℓ state has a biased θ distribution [see Figs. 3(b) and 3(c), and Fig. 4]. This weakly polarized ensemble is transformed by the pump pulse into an ensemble of near-circular trajectories whose angular momentum vectors $\vec{\ell}_T(T_{\rm pump})$ are found within the yz plane but are no longer symmetrically distributed about the origin. This asymmetry allows the polarization of the initial state to be examined.

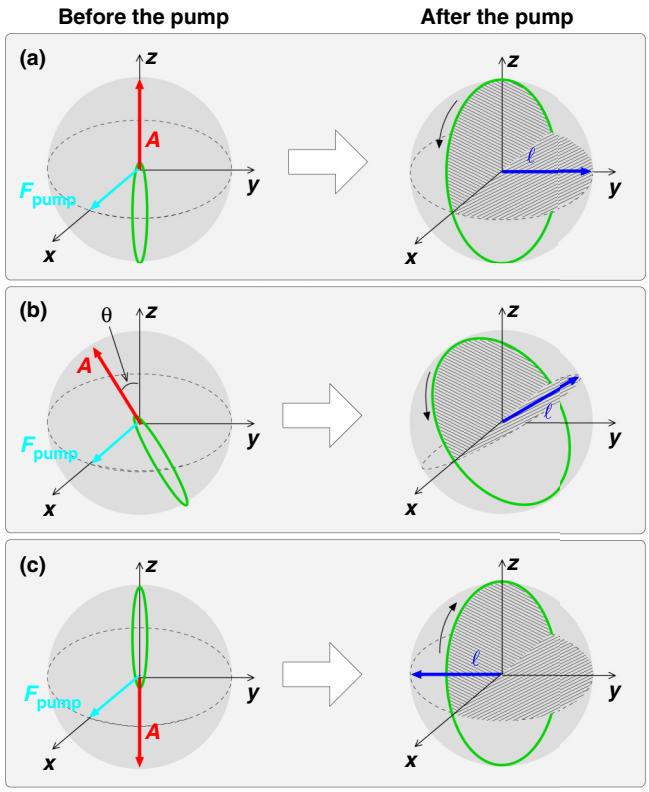

FIG. 7. (Color online) Illustration of circular wave-packet generation. (a),(c) Kepler ellipses (in green) elongated along the z axis are transformed by the pump pulse $F_{\rm pump}$ to circular orbits. Depending on their orientation, the final circular orbit revolves clockwise or anticlockwise in the xz plane. (b) Ellipses oriented at angle θ to the z axis produce circular orbits but not in the xz plane.

One major difficulty in probing stationary high-ℓ states is that they interact only weakly with the probe electric field due to their small dipole moments. However, after the turn-off of $F_{\rm pump}$, the product wave packet can undergo strong transient localization in azimuth, resulting in creation of a localized wave packet that revolves in near-circular, "Bohr-like" orbit about the nucleus and which has a large time-dependent dipole moment (see [16] for more details). The evolution of the wave packet can be readily probed by pulsed-field ionization [Eq. (13)]. To this end, we employ a sequence of two field

steps given by

$$\vec{F}_{\rm ts}(t) = \vec{F}_{\rm pump}(t) + \begin{cases} F_{\rm step}\hat{e} & \text{when} \quad T_{\rm pump} + \tau \leqslant t \leqslant T_{\rm pump} + \tau + T_{\rm step} \\ 0 & \text{otherwise} \end{cases}, \tag{17}$$

which allows the average position of the wave packet to be monitored by varying the time delay τ between the two pulses. Furthermore, by changing the probe field orientation ($\hat{e} = \hat{x}$ or $\hat{z}$), motion parallel ($\langle x(\tau)\rangle$) and transverse ($\langle z(\tau)\rangle$) to the pump field axis can be examined. These expectation values are sensitive to the distribution of $\vec{\ell}$. Since the plane of an orbit is perpendicular to $\vec{\ell}$, the alignment of the angular momentum vectors determines whether the ensemble of orbits is spatially confined within (almost) a two-dimensional plane or is widely distributed in all three dimensions.

For circular wave packets created from well-polarized states, the underlying electron orbits are confined within the xz plane (Fig. 7) and the expectation values $\langle x(\tau)\rangle$ and $\langle z(\tau)\rangle$ undergo strong periodic oscillations,

$$(\langle x(\tau)\rangle, \langle z(\tau)\rangle) \propto (\cos(\omega_n \tau), \sin(\omega_n \tau)), \tag{18}$$

with angular frequency $\omega_n = 2\pi/T_n$. A reduction in oscillation amplitude along the z axis (i.e., perpendicular to the pump pulse) indicates a broader distribution of the planes of orbit (see Fig. 7), implying that the initial state is less well polarized. This behavior is illustrated in the next section and quantified in Sec. VI C.

V. CLASSICAL-QUANTUM HYBRID INITIAL PHASE-SPACE DISTRIBUTION

Fully fledged quantum simulations of the excitation and ionization dynamics for very high-n ($n \sim 300$) Rydberg atoms remain very challenging, even when, as in the case of strontium, the system is reduced to a TAE model. For single-electron systems, such as the alkali atoms, classical simulations have proven to be a powerful tool when analyzing the dynamics of highly excited Rydberg atoms [1] that approach the semiclassical limit. For TAE systems, on the other hand, the classical description can easily fail. For example, even singly excited states can autoionize, since the outer electron may exchange energy with the inner electron for which energies below the ground state are classically accessible. A second, more specific problem for the present classical simulation is how to appropriately represent by a classical ensemble isolated low-ℓ states that are dressed by a dc field (see Fig. 4).

Since singly excited states of strontium with $n > 25$ are well represented using a single inner electron configuration (the $5s$ state), high-n states can be described within a SAE model using the model potential given by Eq. (9). Here we analyze the ionization dynamics using a classical simulation based on a SAE model, thereby avoiding the problem of spontaneous autoionization. In order to properly represent the initial weakly perturbed low-ℓ states, we employ a phase-space distribution derived from the quantum calculations discussed in the following, which we then propagate under the influence of the pump and probe pulses using the classical trajectory Monte Carlo (CTMC) method. The fraction of the ensemble with $E < 0$ at the end of the probe pulse is compared with the measured survival probability.

Since restricted classical microcanonical ensembles fail to properly represent low-ℓ states dressed by a weak dc field $F_{\rm dc}$ (Fig. 4), we employ, instead, ensembles derived from a full quantum calculation to generate the initial conditions for the classical simulations. Accordingly, the initial distribution of the orientations of the low-ℓ Kepler ellipses, i.e., of the polarization, is taken to be the distribution $\rho_{\rm qm}(k)$ (Fig. 4) provided by TAE quantum calculations. We calculate the k distribution for $n \sim 50$ and use scaling relations to generate the distribution for $n \sim 300$ to compare to experiment. In the following, classical simulations using a distribution $\rho_{\rm qm}(k)$ with a fixed value of ℓ are referred to as hybrid-ℓ calculations. For stronger fields, $F_{\rm dc} \simeq F_{\rm cross}$, "$D$" and "$F$" states become indistinguishable from nearby parabolic states. They can thus be treated as a narrow band of parabolic states and represented by a (restricted) microcanonical ensemble with well-defined classical actions n, k, m. These initial conditions are referred to as the parabolic-k distribution in the following. For intermediate field strengths, the measured results are expected to reflect a transition between these two cases. In this regime it is therefore of interest to compare the results of calculations using both these initial ensembles, which should result in a well-defined measure of the polarization irrespective of the uncertainties in the initial k distribution.

We have tested the hybrid-ℓ distribution by comparing results derived from its time evolution with those determined by a full quantum simulation within the TAE model. Since quantum simulations of the ionization induced by the probe pulse are out of reach, we simulate here only the generation and the ensuing evolution of a circular wave packet (with $n = 50$) using the TAE model. As a figure of merit, we use the classical and quantum expectation values of $\langle x(t)\rangle$ and $\langle z(t)\rangle$ when the "$52D$" state is first excited in three typical field strengths $F_{\rm dc}$ and then transformed into a near-circular wave packet (Fig. 8) by a pump pulse $\vec{F}_{\rm pump}$ in the x direction [Eq. (15)]. In all three cases, the quantum mechanically calculated $\langle x(t)\rangle$ (solid lines in the left column) shows that the generated wave packet becomes focused within a few orbital periods, resulting in the buildup of large oscillation amplitudes, which is followed by their collapse as the wave packet disperses. In contrast, the amplitude of the oscillations in $\langle z(t)\rangle$ increases strongly with $F_{\rm dc}$ and becomes comparable to that for $\langle x(t)\rangle$ only when $F_{\rm dc}$ approaches $F_{\rm cross}$. This beating pattern is well reproduced by classical simulations employing the hybrid-ℓ initial distribution (dashed lines). Near the crossing field, $F_{\rm dc} = 0.8 F_{\rm cross}$, the well-polarized "$52D$" state (Fig. 2) is transformed to an ensemble of near-circular orbits, showing strong beat patterns in both $\langle x(t)\rangle$ (bottom left) and $\langle z(t)\rangle$ (bottom right). For weaker $F_{\rm dc}$, the less-polarized initial ensemble is transformed into an ensemble of near-circular states involving two counterpropagating near-circular orbits

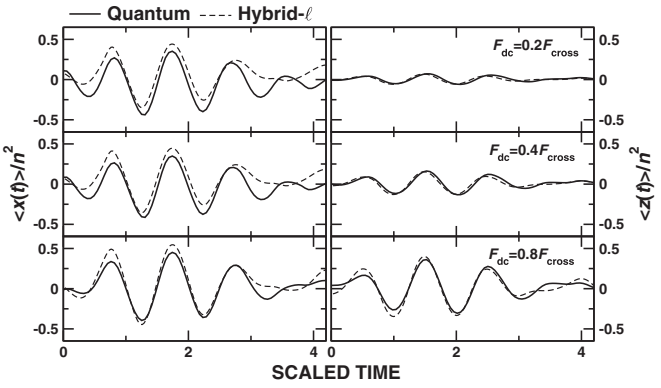

FIG. 8. Calculated expectation values $\langle x(t)\rangle$ and $\langle z(t)\rangle$ for the Bohr wave packet ($n = 50$) generated by a pump pulse with $F_{\rm pump} \simeq 50$ V/cm and $T_{\rm pump} \simeq 52$ ps [Eq. (15)]. The initial state is the "52D" state photoexcited in the presence of a weak dc field $F_{\rm dc}$. The solid lines show the results of quantum simulations using the TAE model [Eq. (6)] and the dashed lines the results of CTMC simulations [Eqs. (1) and (9)] employing the hybrid-ℓ distribution as the initial condition.

with $\ell_{T,y}(T_{\rm pump}) = -n$ and $\ell_{T,y}(T_{\rm pump}) = n$ [see Eq. (16) and Figs. 7(a) and 7(c)]. Because the planes of these orbits share the x axis (i.e., the axis parallel to the pump pulse) [Eq. (16) and Fig. 7(b)], when an ensemble average is taken, contributions from the different orbits to $\langle x(t)\rangle$ reinforce each other while their contributions to $\langle z(t)\rangle$ cancel due to the presence of counterpropagating components. Given the satisfactory agreement between the quantum-mechanical and CTMC results, we now proceed to analyze the experimental results obtained using the different probing schemes.

VI. COMPARISON WITH EXPERIMENT

A. Pulsed field ionization

We first discuss the electronic polarization as determined by pulsed field ionization [Eq. (12)]. Figure 9 shows the survival probabilities measured as a function of probe field amplitude $F_{\rm step}$ and direction (▲ for $F_{\rm step} > 0$ and ▼ for $F_{\rm step} < 0$) for "312D" states excited in different dc fields, $F_{\rm dc}$. The present results were recorded using $T_{\rm step} = 10$ ns $\simeq 2.3T_n$. The figure also includes the results of CTMC simulations, employing both the hybrid-ℓ and the parabolic-k distributions as initial conditions. For both distributions the strength of the probe pulse $F_{\rm step}$ required for ionization of the uphill states depends markedly on $F_{\rm dc}$. For these states, the hybrid-ℓ distribution yields larger survival probabilities than the parabolic-k distribution, because the latter involves high-ℓ states whose orbits extend to the downhill side, leading to an increased ionization probability. On the other hand, the ionization characteristics of the downhill states are rather insensitive to the value of $F_{\rm dc}$ and the initial ensemble. This results because those electrons with energies above the Stark saddle can readily escape over it. For $F_{\rm dc} \leqslant 0.6F_{\rm cross}$, the results employing the hybrid-ℓ distribution agree well with the measured data while the calculations performed with the parabolic-k distribution agree better with the measured results for $F_{\rm dc} \geqslant 0.6F_{\rm cross}$. Since the parabolic-$k$ distribution

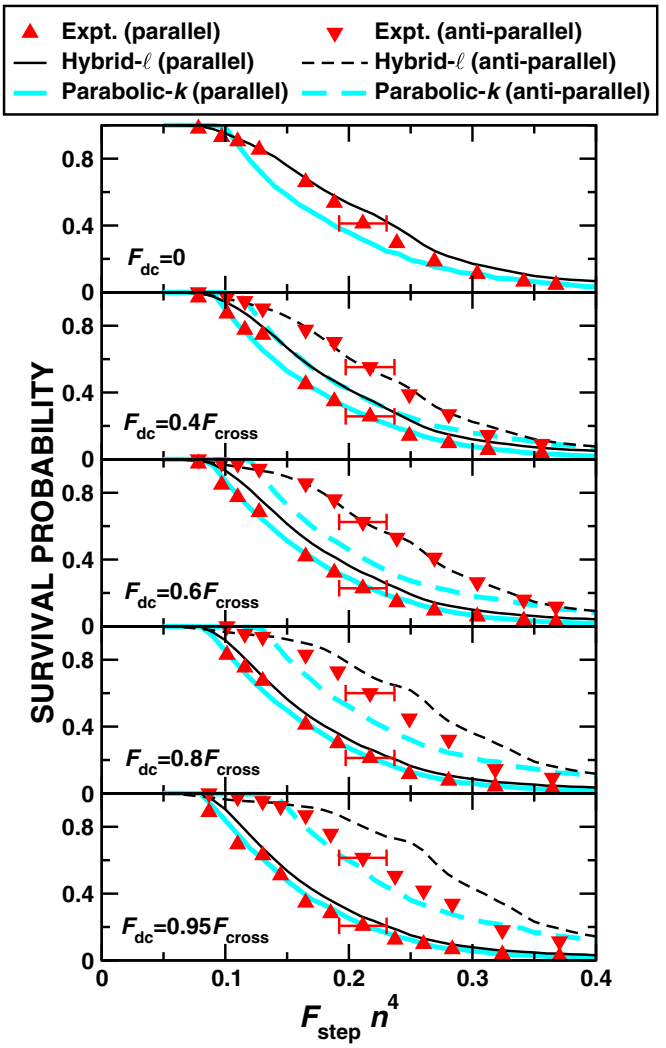

FIG. 9. (Color online) Measured ionization probabilities for "312D" states excited in the dc fields, indicated as a function of the scaled amplitude of a probe field $F_{\rm step}$ of 10-ns duration, $T_p \sim 2.3T_n$. Symbols denote data points recorded with the probe field applied parallel (▲) and antiparallel (▼) to the dc electric field, $F_{\rm dc}$. Calculated ionization probabilities for the "312D" states obtained using the hybrid-ℓ and the parabolic-k distributions are shown by the black and light-blue (gray) lines, respectively. Solid (dashed) lines are for the probe field parallel (antiparallel) to $F_{\rm dc}$. The error bars indicate the 10% uncertainty in $F_{\rm step}$.

assumes near-parabolic states while the hybrid-ℓ distribution is designed to represent a state with fixed angular momentum ℓ of the outer electron, this experimental observation indicates a transition from a state with weak ℓ-mixing to one with strong ℓ-mixing as $F_{\rm dc}$ is increased.

We have further tested this probing scheme through measurements undertaken using the neighboring "312P" state at $F_{\rm dc} \sim 0.6F_{\rm cross}$. The data revealed little asymmetry, consistent with the predicted weak polarization [Fig. 2(b)]. In a further test the 413-nm laser was tuned to excite extreme blue-shifted Stark states lying near the top of the $n = 309$ manifold in a field $F_{\rm dc} \sim 0.9F_{\rm cross}$. Although the signal levels were low, the data revealed a noticeable asymmetry in the opposite sense to

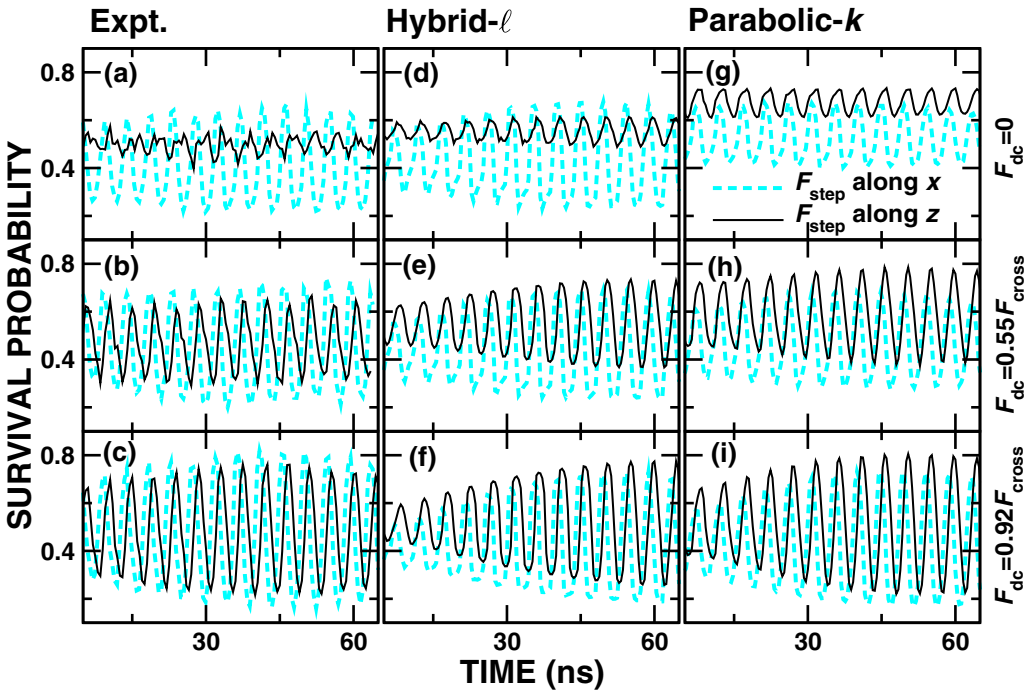

FIG. 10. (Color online) (a)–(c) Survival probabilities measured for "312D" states produced in the dc field indicated and subject to a 5 mV cm^{-1}, 80-ns-long pump pulse as a function of the time delay between the end of the pump pulse and application of a 6-ns-long probe pulse $F_{\rm step}$(=120 mV cm^{-1} when probing along the x axis and 105 mV cm^{-1} when probing along the z axis), together with the corresponding simulations employing the hybrid-ℓ (d)–(f) and the parabolic-k (g)–(i) distributions. The black (light blue/gray) lines correspond to application of the probe pulse in the z (x) directions. The applied dc fields are (a),(d),(g) $F_{\rm dc} = 0$, (b),(e),(h) 300 μV cm^{-1}, and (c),(f),(i) 500 μV cm^{-1}.

that seen for red-shifted states, consistent with the creation of states with opposite polarization.

B. Production of circular states

In the second series of experiments, creation of circular wave packets is explored. In these experiments, "312D" states were subject to a 5 mV cm^{-1}, 80-ns-long pump pulse followed by application of a 6-ns-long probe pulse of amplitude $F_{\rm step} =$ 120 mV cm^{-1} when probing along the x axis and 105 mV cm^{-1} when probing along the z axis. As a function of the time delay τ between the pump and probe pulses [Eq. (17)], the measured survival probabilities [Figs. 10(a)–10(c)] and the calculated probabilities employing the hybrid-ℓ [Figs. 10(d)–10(f)] and the parabolic-k [Figs. 10(g)–10(i)] distributions mirror the expectation values $\langle x(t)\rangle$ and $\langle z(t)\rangle$. Similar to Fig. 8, transient localization leading to the buildup of strong oscillations in the survival probability is clearly seen, particularly in panels (c), (f), and (i). (We note in passing that due to more equispaced energy levels at $n \simeq 312$ compared to $n \simeq 50$, the wave packet involving different n levels evolves more coherently, thus increasing the number of orbital periods required to build up large "quantum beat" amplitudes [29].) When probing in the x direction, the measured oscillation amplitudes are largely independent of the size of the applied dc field $F_{\rm dc}$. Even when $F_{\rm dc} = 0$, i.e., for an unpolarized 312D initial state, large beat amplitudes are seen reflecting large periodic changes in the survival probability. This is to be expected, as all orbits share the x axis (Sec. IV B) and contribute to the large oscillation in $\langle x(t)\rangle$. In contrast, when probing along the z direction, the amplitude of the oscillation depends markedly on $F_{\rm dc}$ and increases steadily with increasing $F_{\rm dc}$. Finally, for $F_{\rm dc} \sim F_{\rm cross}$, the oscillations in $\langle z(t)\rangle$ are comparable in amplitude to those seen in $\langle x(t)\rangle$ but are 90° out of phase [Eq. (18)], perfectly consistent with the creation of a localized wave packet moving in a near-circular Bohr-like orbit. The hybrid-ℓ distribution reproduces the measured results reasonably well, particularly for weak $F_{\rm dc}$ [Figs. 10(d) and 10(e)]. Even though the initial Rydberg state evolves towards a parabolic state with increasing $F_{\rm dc}$, the CTMC simulations using the parabolic-k distribution perform only slightly better than those employing the hybrid-ℓ distribution. We return to this point below.

C. Determining the dipole moment

For each of the two probing schemes outlined above the observed asymmetries increase with applied dc field, consistent with an increase in the polarization of the photoexcited "nD" states. The key question remains, however, as to just how well can the polarization and average dipole moment of an initial state be determined from the magnitude of the measured asymmetries? To this end, we define the asymmetry for ionization by a pulsed field as the difference between the survival probabilities measured with probe fields applied parallel and antiparallel to the dc field. We pick the value for the field strength $|F_{\rm step}|$ as 110 mV cm$^{-1} \simeq 0.2/n^4$, where the observed asymmetry is prominent. In analyzing the data for a circular (Bohr) wave packet, we consider the maximum amplitude of oscillation in the survival probabilities. Since only oscillation amplitudes in the z direction, i.e., transverse to the pump pulse, display a sizable dependence on $F_{\rm dc}$, we focus on $\langle z(t)\rangle$ as a measure for the polarization.

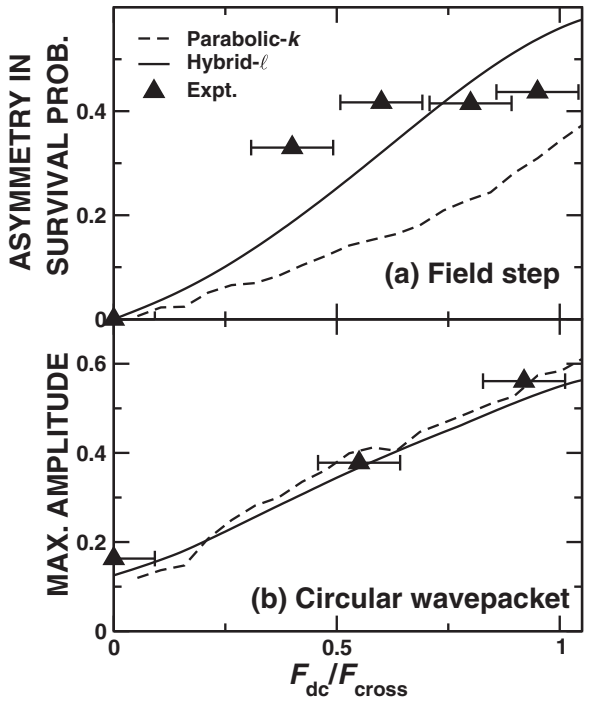

FIG. 11. (a) The asymmetry, i.e., the differences in survival probability, between positive and negative probe pulses derived from Fig. 9. (b) Peak amplitude of the oscillations in survival probability observed when probing along the z axis following creation of circular wave packets, taken from Fig. 10. ▲ : measurements, ——: calculations using the hybrid-ℓ ensemble, and - - - : using the parabolic-k distribution. The error bars correspond to stray fields of $\sim 50\ \mu\mathrm{V\,cm^{-1}}$.

Figure 11 displays the asymmetries measured as a function of F_{dc} for each of the two probing schemes. Since for a given value of F_{dc}, the initial hybrid-ℓ and parabolic-k ensembles employed in the simulations have, by design, the same electric dipole moment, the simulations might be expected to yield similar ionization asymmetries if these are, indeed, controlled by the dipole moment alone. This, however, seems only to be true for the predicted maximum oscillation amplitude following generation of a circular wave packet, which thus appears to provide a direct and unambiguous measure of the dipole moment [see Fig. 11(b)]. In contrast, simple ionization by a field step [see Fig. 11(a)] yields simulated asymmetries that depend on the initial ensemble. This implies that these asymmetries probe not only the dipole moment, i.e., the first moment, but also the higher moments of these distributions. One key difference between the two probing schemes is that measurement of the maximum amplitude of the oscillations in survival probability for circular wave packets [see Fig. 10] probes the time-dependent response, i.e., the Fourier amplitude, near the Stark precession frequency ω_S, while the second probes the zero-frequency (or static) response. The latter is apparently more sensitive to properties of the initial distribution beyond the first moment. This point is corroborated by the observation that even in the case of circular wave packets (Fig. 10), the calculated time-averaged survival probabilities, i.e., the zero-frequency response (unlike the oscillation amplitude) depends on the choice of the initial ensemble. We note that the polarization of the target state was also examined using a third probing protocol that employed a periodic train of 20 half-cycle pulses (HCPs) applied parallel and antiparallel to the polarization axis [30]. Large asymmetries in the survival probabilities were observed and the data again suggested a dependence on higher-order moments.

For pulsed-field ionization [Fig. 11(a)], calculations using the hybrid-ℓ distribution predict a larger asymmetry than those based on the parabolic-k distribution. This difference in asymmetry reflects the relative weights of high-ℓ and low-ℓ states in the initial ensemble. Because high-ℓ states extend their orbits more symmetrically on both sides of the nucleus, their contributions to the asymmetry in survival probability are expected to be smaller than those for low-ℓ states. Since the parabolic-k distribution has a broad ℓ distribution that extends to high ℓ values while the initial hybrid-ℓ ensemble includes only $\ell = 2$ states, this accounts for the observed differences [Fig. 11(a)] in the predicted asymmetries. The measured asymmetry agrees better with the hybrid-ℓ simulations at small F_{dc}, while near $F_{\mathrm{dc}} = F_{\mathrm{cross}}$ the agreement with the parabolic-k simulations improves, which is consistent with the experimentally generated state transitioning from a narrowly peaked $\ell = 2$ distribution to a broad-ℓ distribution.

Overall, the amplitude of the oscillations in survival probability following creation of a near-circular wave packet [Fig. 11(b)] emerges as the most robust and unambiguous measure for the first moment of $\rho_{\mathrm{qm}}(k)$, i.e., the dipole moment of the photoexcited state. At $F_{\mathrm{dc}} = 0.5F_{\mathrm{cross}}$ ($0.9F_{\mathrm{cross}}$), comparison of the measured oscillation amplitudes to simulations using the hybrid-ℓ (parabolic-k) distribution point to a dipole moment $\langle d \rangle = 0.6n^2$ ($1.2n^2$). The biggest advantage of this probing scheme is that the dipole moment can be determined even when the distribution $\rho_{\mathrm{qm}}(k)$ is not available, i.e., an ensemble of parabolic states can simply be determined that best fits the measured oscillation amplitudes. Additionally, since the evolution of near-circular wave packets is rather insensitive to the core potential, the CTMC simulations can be performed using the Coulomb potential instead of a more-complex model potential.

VII. SUMMARY

The present work demonstrates that strongly polarized quasi-1D high-n strontium Rydberg atoms can be created by two-photon excitation in an applied dc field $F_{\mathrm{dc}} \sim F_{\mathrm{cross}}$ and their polarization probed by pulsed field ionization and by creation of near-circular wave packets. Also, the experimental data can be analyzed with the aid of CTMC simulations that use different ensembles to represent the initial photoexcited state. This initial state was calculated using a TAE model which also served to validate the CTMC dynamics for the creation of circular wave packets. The analysis protocols used probe not only the average dipole moment of the photoexcited Rydberg states but also the effects of core scattering and the role of ℓ mixing. The product states were shown to have large dipole moments of ~ 1.0–$1.2n^2$ and can be engineered using pulsed electric fields to create a wide variety of target states, including near-circular Bohr-like atoms and strongly correlated two-electron-excited states.

ACKNOWLEDGMENTS

This research is supported by the NSF under Grants No. 0964819 and No. 1301773, the Robert A. Welch Foundation under Grant No. C-0734, by the FWF (Austria) under Grant No. P23359-N16, and SFB-NextLite. The Vienna Scientific Cluster was used for the calculations.

[1] F. B. Dunning, J. J. Mestayer, C. O. Reinhold, S. Yoshida, and J. Burgdörfer, J. Phys. B **42**, 022001 (2009).

[2] A. Buchleitner, D. Delande, and J. Zakrzewski, Phys. Rep. **368**, 409 (2002).

[3] R. V. Jensen, S. M. Susskind, and M. M. Sanders, Phys. Rep. **201**, 1 (1991).

[4] D. Delande and J. C. Gay, Europhys. Lett. **5**, 303 (1988).

[5] F. B. Dunning, C. O. Reinhold, S. Yoshida, and J. Burgdörfer, Am. J. Phys. **78**, 796 (2010).

[6] D. A. Anderson, A. Schwarzkopf, R. E. Sapiro, and G. Raithel, Phys. Rev. A **88**, 031401 (2013).

[7] J. Murray-Krezan, J. Kelly, M. R. Kutteruf, and R. R. Jones, Phys. Rev. A **75**, 013401 (2007).

[8] A. V. Gorshkov, A. M. Rey, A. J. Daley, M. M. Boyd, J. Ye, P. Zoller, and M. D. Lukin, Phys. Rev. Lett. **102**, 110503 (2009).

[9] G. Lochead, D. Boddy, D. P. Sadler, C. S. Adams, and M. P. A. Jones, Phys. Rev. A **87**, 053409 (2013).

[10] P. McQuillen, X. Zhang, T. Strickler, F. B. Dunning, and T. C. Killian, Phys. Rev. A **87**, 013407 (2013).

[11] M. Kalinski, J. H. Eberly, J. A. West, and C. R. Stroud, Phys. Rev. A **67**, 032503 (2003).

[12] U. Eichmann, V. Lange, and W. Sandner, Phys. Rev. Lett. **68**, 21 (1992).

[13] K. Richter and D. Wintgen, Phys. Rev. Lett. **65**, 1965 (1990).

[14] C. L. Stokely, J. C. Lancaster, F. B. Dunning, D. G. Arbó, C. O. Reinhold, and J. Burgdörfer, Phys. Rev. A **67**, 013403 (2003).

[15] B. E. Tannian, C. L. Stokely, F. B. Dunning, C. O. Reinhold, and J. Burgdörfer, Phys. Rev. A **64**, 021404 (2001).

[16] J. J. Mestayer, B. Wyker, J. C. Lancaster, F. B. Dunning, C. O. Reinhold, S. Yoshida, and J. Burgdörfer, Phys. Rev. Lett. **100**, 243004 (2008).

[17] P. Esherick, Phys. Rev. A **15**, 1920 (1977).

[18] M.-c. Zhi, C.-j. Dai, and S.-b. Li, Chin. Phys. **10**, 929 (2001).

[19] J. Millen, G. Lochead, G. R. Corbett, R. M. Potvliege, and M. P. A. Jones, J. Phys. B **44**, 184001 (2011).

[20] S. Ye, X. Zhang, T. C. Killian, F. B. Dunning, M. Hiller, S. Yoshida, S. Nagele, and J. Burgdörfer, Phys. Rev. A **88**, 043430 (2013).

[21] M. Born, *The Mechanics of the Atom* (G. Bell and Sons, London, 1927).

[22] T. P. Hezel, C. E. Burkhardt, M. Ciocca, L.-W. He, and J. J. Leventhal, Am. J. Phys. **60**, 329 (1992).

[23] A. R. P. Rau, Rep. Prog. Phys. **53**, 181 (1990).

[24] K. Molmer and K. Taulbjerg, J. Phys. B **21**, 1739 (1988).

[25] E. Luc-Koenig, M. Aymar, J.-M. Lecomte, and A. Lyras, J. Phys. B **31**, 727 (1998).

[26] J. E. Sansonetti and G. Nave, J. Phys. Chem. Ref. Data **39**, 033103 (2010).

[27] C. L. Vaillant, M. P. A. Jones, and R. M. Potvliege, J. Phys. B **45**, 135004 (2012).

[28] I. C. Percival and D. Richards, J. Phys. B **12**, 2051 (1979).

[29] B. Wyker, S. Ye, F. B. Dunning, S. Yoshida, C. O. Reinhold, and J. Burgdörfer, Phys. Rev. A **84**, 043412 (2011).

[30] C. O. Reinhold, W. Zhao, J. C. Lancaster, F. B. Dunning, E. Persson, D. G. Arbó, S. Yoshida, and J. Burgdörfer, Phys. Rev. A **70**, 033402 (2004).